AIF translocation into nucleus caused by *Aifm1* R450Q mutation: generation and characterization of a mouse model for AUNX1

Tao Shi[1,2,†], Ziyi Chen[1,2,†], Jin Li[1,2], Hongyang Wang[1,2,*], Qiuju Wang (iD)[1,2,*]

[1]Senior Department of Otolaryngology-Head and Neck Surgery, the Sixth Medical Center of PLA General Hospital, Medical School of Chinese PLA, 6 Fucheng Road, Beijing 100048, P. R. China
[2]National Clinical Research Center for Otolaryngologic Diseases, Chinese PLA General Hospital, 6 Fucheng Road, Beijing 100048, P. R. China
*Corresponding authors. Senior Department of Otolaryngology-Head and Neck Surgery, the Sixth Medical Center of PLA General Hospital, Medical School of Chinese PLA, 6 Fucheng Road, Beijing 100048, P. R. China. E-mail: whyx301@foxmail.com and Senior Department of Otolaryngology-Head and Neck Surgery, the Sixth Medical Center of PLA General Hospital, Medical School of Chinese PLA, 6 Fucheng Road, Beijing 100048, P. R. China. E-mail: wqjavm301@sina.com; wqcr301@vip.sina.com
[†]Tao Shi & Ziyi Chen contributed equally.

Abstract

Mutations in *AIFM1*, encoding for apoptosis-inducing factor (AIF), cause AUNX1, an X-linked neurologic disorder with late-onset auditory neuropathy (AN) and peripheral neuropathy. Despite significant research on AIF, there are limited animal models with the disrupted *AIFM1* representing the corresponding phenotype of human AUNX1, characterized by late-onset hearing loss and impaired auditory pathways. Here, we generated an *Aifm1* p.R450Q knock-in mouse model (KI) based on the human *AIFM1* p.R451Q mutation. Hemizygote KI male mice exhibited progressive hearing loss from P30 onward, with greater severity at P60 and stabilization until P210. Additionally, muscle atrophy was observed at P210. These phenotypic changes were accompanied by a gradual reduction in the number of spiral ganglion neuron cells (SGNs) at P30 and ribbons at P60, which coincided with the translocation of AIF into the nucleus starting from P21 and P30, respectively. The SGNs of KI mice at P210 displayed loss of cytomembrane integrity, abnormal nuclear morphology, and dendritic and axonal demyelination. Furthermore, the inner hair cells and myelin sheath displayed abnormal mitochondrial morphology, while fibroblasts from KI mice showed impaired mitochondrial function. In conclusion, we successfully generated a mouse model recapitulating AUNX1. Our findings indicate that disruption of *Aifm1* induced the nuclear translocation of AIF, resulting in the impairment in the auditory pathway.

Graphical Abstract
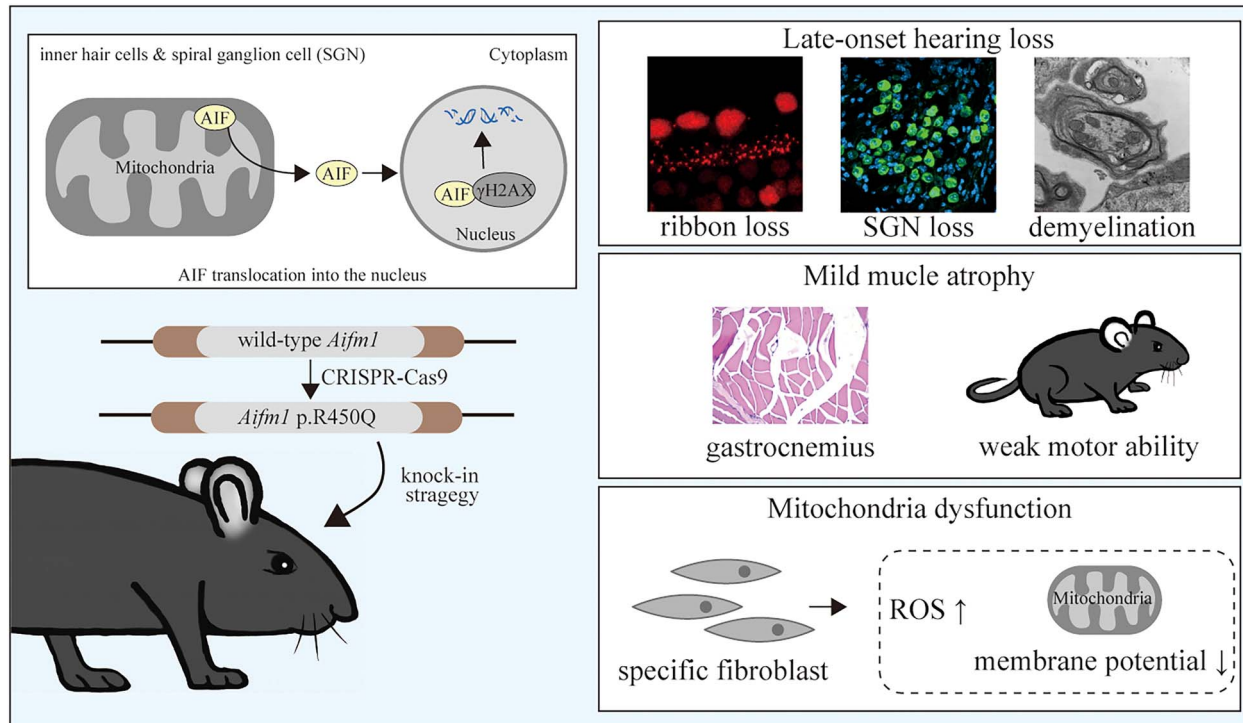
A novel mouse model with *Aifm1* R450Q mutation representing the AUNX1 phenotype was successfully generated.

Keywords: AIFM1; AIF; mouse; auditory neuropathy; demyelinating disease

Introduction

Hearing loss is one of the most severe public health issues in some counties or regions. Auditory neuropathy (AN) is a complex hearing disorder characterized by difficulties in processing speech information. It is a refractory condition that results in hearing and speech communication disorders among infants and adolescents, constituting 10% of permanent hearing loss cases in children [1, 2]. As a global challenge and research hotspot, studies have been investigating AN since the 1990s [3–6]. Clinical research and animal models have demonstrated that AN involves a diverse array of pathogenic mechanisms, which might affect the inner hair cells (IHCs), synapses between the IHCs and the auditory nerve, spiral ganglion neuron cells (SGNs), and auditory nerve fibers [5]. The etiology of AN is also multifactorial, with genetic factors, accounting for 40%, and the rest comprises other environmental factors like noise exposure, ototoxic drugs, and hyperbilirubinemia [7]. Previously, we identified *AIFM1* (NM_004208.3: c.1352G>A, p.R451Q) as a causal gene for AUNX1 (OMIM: #300614), an X-linked disorder primarily characterized by AN [8, 9]. *AIFM1* is commonly associated with late-onset AN, accounting for 18.6% of AN cases in the Chinese population [10]. To the best of our knowledge, its prevalence in other countries and populations has not been identified yet. Most studies on *AIMF1* variations have been documented as case studies worldwide.

So far, besides AUNX1, other two *AIFM1*-related genetic diseases have been identified. *AIFM1* c. del 601-603 (p.R201 del) was reported in two Italian male infants affected by severe oxidative phosphorylation (OXPHOS) deficiency and mitochondrial encephalomyopathy named Combined Oxidative Phosphorylation Deficiency 6 (COXPD6) [11]. Charcot-Marie-Tooth Disease 4 (CMT4X) or Cowchock syndrome is another *AIFM1*-related genetic disease. Patients with CMT4X exhibit childhood-onset limb ataxia, hearing loss, and cognitive impairment. In adolescence, they additionally manifest visual deficits, distal muscle wasting and weakness [12, 13]. Although the characteristics of various diseases may differ, alterations in mitochondrial function and energy metabolism are commonly observed among patients, affecting multiple tissues or organs [14].

AIFM1 encodes apoptosis-inducing factor (AIF), initially believed to induce caspase-independent apoptosis [15]. Subsequent studies revealed that AIF is crucial for parthanatos [16], a regulated cell death (RCD) that is similar to both apoptosis and necrosis [17]. AIF is regulated by poly (ADP-ribose) polymerase 1 and translocated to the nucleus, resulting in chromatin condensation and large-scale DNA fragmentation [18]. In the nucleus, the binding of AIF and Ser139-phosphorylated H2AX (γH2AX) is a key event [19, 20]. Parthanatos has been implicated in the pathogenesis of diverse neurodegenerative disorders [21]. Notably, AIF plays a distinct role in the nucleus and mitochondria. AIF is a mitochondrial flavin adenine dinucleotide-dependent oxidoreductase essential in OXPHOS and redox control in healthy cells [22]. It also maintains the function and morphology of respiratory complexes, ensuring proper mitochondrial function [23, 24].

Due to the specific functions of AIF, its involvement in these two opposing processes has been extensively studied [22, 25], using several animal or cellular models of disease, like Harlequin (Hq) mutant mice [26–30]. As the Hq mice do not possess a pure genetic background and exhibit significant individual variations in terms of body weight, growth retardation, fur abnormalities, and neurological symptoms [30], they are valuable *in vivo* models for studying mitochondrial disorders associated with Complex I deficiency. Because Hq mutant mice are AIF dysfunction models rather than specifically designed to mimic *AIFM1* disruption, developing animal models that accurately recapitulate the precise molecular pathogenesis of *AIFM1* mutations is necessary. The initial *Aifm1* knock-in (KI) mouse model was based on human *AIFM1* p.R201 del and harbored many pathological features similar to those observed in patients with COXPD6, such as myopathy, peripheral degeneration and severe damage to skeletal muscle complexes I and IV [31]. However, currently, there are no animal models that accurately mimic AUNX1, and therefore, the research on the role of *AIFM1* disruption in impairing hearing function and pathogenic auditory pathways in KI animal models is limited.

To better understand the role of *AIFM1* in AN and auditory pathways, we generated an *Aifm1* p.R450Q KI mouse model based on the human *AIFM1* p.R451Q mutation using CRISPR-Cas9. The KI mice exhibited late-onset hearing loss and muscle atrophy along with impaired auditory pathway functions. *Aifm1* mutation resulted in mitochondrial dysfunction and the translocation of AIF into the nucleus. Thus, we successfully generated the *Aifm1* KI mouse model with AN phenotype, which elucidates the underlying mechanism of *AIFM1*-related AN and provides a foundation for future gene or drug therapy.

Results

Generation and molecular characterization of *Aifm1* (p.R450Q) knock-in mice

AIFM1 mutation c.1352G>A (p.R451Q) in humans was associated with AUNX1 [9]. Previously, we identified this mutation in a four-generation Chinese family exhibiting phenotypic characteristics of AN (Fig. 1A) [8]. As Arg451 (NP_004199.1) in AIF was highly conserved between several species (Supplementary Material 1, Fig. S1A), we generated a mouse model carrying the synthetic amino acid alteration. Using sequence alignment, we identified that Arg450 (NP_036149.1) in the mouse AIF is homologous to the human Arg451 (Supplementary Material 1, Fig. S1B). *Aifm1* (p.R450Q) KI mice were generated by the CRISPR-Cas9 system (Fig. 1B). Mutations in *AIFM1* on the X chromosome cause its disruption. The phenotypes of male patients with *AIFM1* mutations remained consistent. However, there were phenotypic differences between female carriers with *AIFM1* mutations (heterozygote). The vast majority of female carriers demonstrated normal auditory function, while only a minority of female carriers exhibited hearing loss [10]. Therefore, to avoid the potential bias introduced by X-inactivation, the animals analyzed here were hemizygous *Aifm1* KI male mice and littermate wild-type (WT) CBA/CaJ male mice. Western blot (WB) analysis of the cochlea revealed that the expression levels of AIF were lower in P30 KI mice compared to WT mice (Fig. 1D).

To explore the role of AIF in auditory function, we examined its expression in the mouse cochlea. Immunostaining of the cryosection of P30 WT mouse cochlear hair cells (Fig. 1E and F) revealed widespread expression of AIF throughout the cochlea, including IHCs, outer hair cells (OHCs), SGNs, and stria vascularis (SV).

Aifm1 (p.R450Q) knock-in mice have late-onset hearing loss and muscle atrophy

To investigate the impact of *Aifm1* mutation on auditory function and verify the AN phenotype, we conducted auditory brainstem response (ABR) and distortion products of otoacoustic emission (DPOAE) on KI mice. The KI mice exhibited progressive hearing loss with delayed onset as indicated by ABR (Fig. 2B). Although initially indistinguishable in the WT and KI mice at P21 (Fig. 2D), the thresholds of 24 and 32 kHz gradually increased in KI mice at P30 (n = 29 ears, 25.52 ± 14.70 dB SPL for 24 kHz in KI, $P = 0.0001$; 24.48 ± 12.96 dB SPL for 32 kHz in KI, $P = 0.0032$; compared to age-matched WT) (Fig. 2E). At P60, the thresholds were further increased at all frequencies (n = 15 ears, 34.67 ± 9.91, 30.33 ± 12.45, 30.67 ± 13.89, 38.00 ± 15.36, 49.00 ± 13.93 dB SPL respectively for KI mice compared to age-matched WT; $P = 0.0053$, $P = 0.0059$, $P = 0.0049$, $P = 0.0001$, $P < 0.0001$, respectively) (Fig. 2F). The ABR threshold in KI mice remained stable until P210 (n = 21 ears, 39.05 ± 15.48, 30.71 ± 15.30, 32.62 ± 14.28, 45.71 ± 16.13, 46.19 ± 17.65 dB SPL for all frequencies compared to age-matched WT; $P < 0.0001$, $P = 0.0058$, $P = 0.0006$, $P < 0.0001$, $P < 0.0001$, respectively) with extremely poorly differentiated waveforms. DPOAE was indistinguishable between WT and KI mice at several ages with the oldest being at P270 (Fig. 2A). Meanwhile, the suprathreshold amplitude of the ABR wave I declined in KI mice (Fig. 2C and Supplementary Material 1, Fig. S2).

Additionally, KI mice exhibited hind limb clasping at P270, indicating potential late-onset muscle atrophy. The abnormal motor function (Fig. 2J–L) and muscle atrophy observed at P210 (Fig. 2M) indicated skeletal muscle abnormalities. However, these mice did not show any obvious signs within the cerebellum (Fig. 2I).

### *Aifm1* (p.R450Q) knock-in mice have multiple impairments in the auditory pathway

As KI mice showed a delayed onset of hearing impairment, we further investigated the underlying cause of the apparent threshold shift observed at P60. To confirm the potential damage to the auditory pathway, we quantified SGNs and presynaptic ribbons (CtBP2) in the cochlea of KI mice using confocal imaging.

We evaluated the presynaptic ribbons of IHCs, which are essential for processing auditory information and potential pathogenic sites for AN. While no reduction in ribbon numbers at P21 and P30, a significant decrease was detected at the basal turn at P60 in KI (n = 3 ears from different mice, 7.03 ± 1.14 for per IHCs of KI; compared to age-matched WT, n = 7 ears, 11.44 ± 1.33 for per IHCs, $P = 0.0004$). The ribbons at the whole turn in KI mice were less than those observed in WT mice at P210 (n = 9 ears, the apical, middle, basal turn in KI were 7.82 ± 0.88, 11.85 ± 1.40, 6.79 ± 2.06, respectively; compared to age-matched WT, n = 6–11 ears, 11.37 ± 1.06, 15.06 ± 1.12, 10.92 ± 1.95, $P < 0.0001$, $P < 0.0001$, $P < 0.0001$, respectively) (Fig. 3B).

Post-synaptic and auditory nerve fibers are vital for the auditory pathway as they transmit and convert information from the IHCs. Therefore, we examined the density of SGNs. At P30, immunofluorescence staining showed that the number of SGNs at the basal turn of KI mice lower than that in the WT mice (n = 6 ears, 23.98 ± 2.55 for KI; compared to age-matched WT, n = 8 ears, 34.16 ± 3.72, $P < 0.0001$). In KI mice, the SGNs of whole cochlear was significantly decreased at P210 (n = 9, the apical, middle, and basal turn of KI were 24.12 ± 3.62, 25.08 ± 2.88, 19.44 ± 3.18 respectively; compared to age-matched WT, n = 10 ears, 36.17 ± 3.01, 35.42 ± 3.96, 33.16 ± 5.21, $P < 0.0001$, $P < 0.0001$, $P < 0.0001$, respectively) (Fig. 4C).
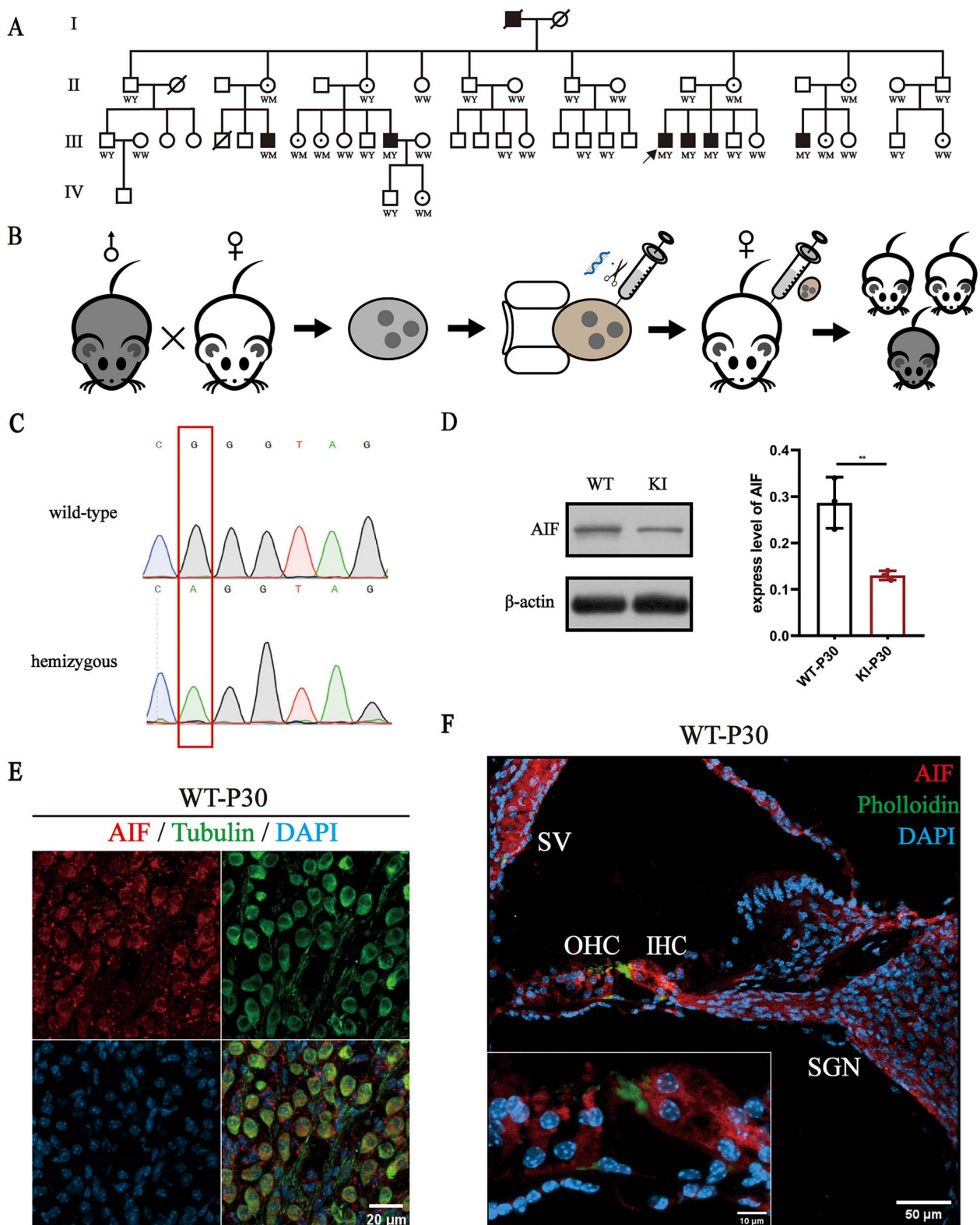
Figure 1. Generation of *Aifm1* (p.R450Q) knock-in (KI) mice and cochlear expression of AIF. (A) The pedigree of the *AIFM1*-related auditory neuropathy family showing the genotypes of c.1352 locus for each member. WY or WW means hemizygous or homozygous for the wild-type (WT) sequences, WM means heterozygous, and MY means the mutation in hemizygous. The arrowhead and slashes in black refer to the proband and death, respectively. The pedigree has been published previously [9]. (B) Schematic of the generation of KI mice. Briefly, guide RNAs and Cas9 mRNA were co-injected into the zygotes and then injected into the uterus of pseudo-pregnant female mice. KI mice were then bred for subsequent experiments (Supplementary Material 2). ♂: male, ♀: female. (C) The sequence results showed that the WT on the top, and mutation (hemizygote) on the bottom. (D) Left panel: Protein expression of AIF by using Western blot at P30. Right panel: Relative protein expression levels of AIF. β-actin was used as the loading control. All experiments were replicated in triplets. ** means $P < 0.01$. (E) Immunofluorescence staining of AIF, tubulin, and DAPI in the spiral ganglion neuron (SGN) of the WT mice at P30. Scale bar = 20 μm. (F) Immunofluorescence staining of AIF, phalloidin, and DAPI in the cochlea of the WT mice at P30. Scale bar = 50 μm. OHC: outer hair cells; IHC: inner hair cells; SGN: spiral ganglion neuron; SV: stria vascularis.
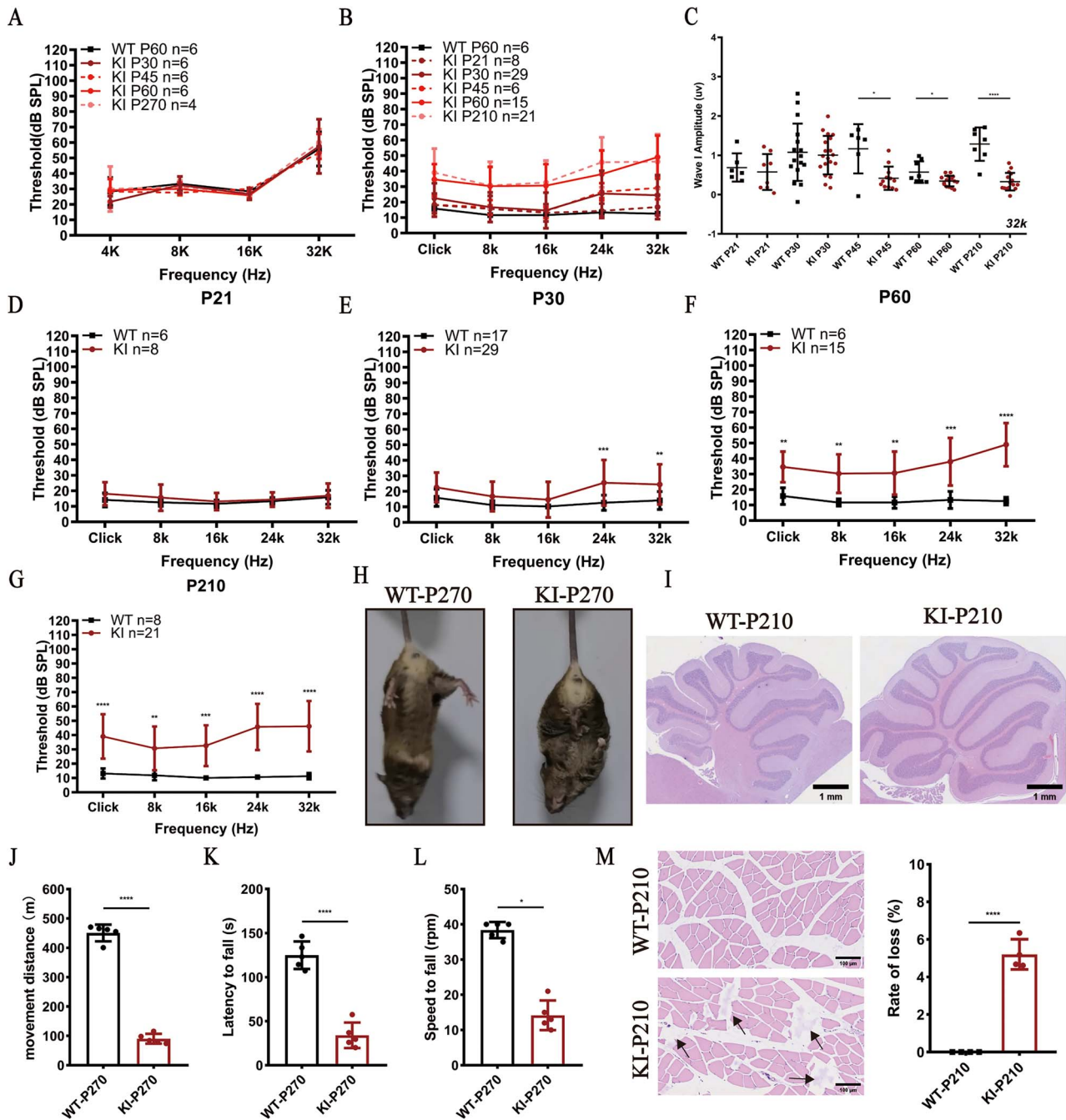
Figure 2. *Aifm1* (p.R450Q) knock-in (KI) mice exhibited late-onset hearing loss and muscle atrophy. (A) Indistinguishable distortion product otoacoustic emission (DPOAE) thresholds of the wild-type (WT) and KI mice (n represents ears). (B) From P21 to P210, KI mice showed progressive hearing loss in the auditory brainstem response (ABR) threshold (n represent ears). (C) Significantly declined ABR wave-I amplitude at 80 dB SPL at frequencies of 32 kHz at all ages. Wave-I amplitude decreased in KI mice from P45 compared to WT mice (n represent ears. WT, n = 6–17. KI, n = 8–19.) (other frequencies are available in Supplementary Material 1 Fig. S2). (D–G) Dynamic analysis of the ABR threshold. Indistinguishable ABR thresholds of the WT and KI mice at P21. ABR thresholds was significantly elevated at frequencies of 24 and 32 kHz at P30 and further elevated at all frequencies at P60. At P210, the ABR threshold was indistinguishable from P60. ** means $P < 0.01$, *** means $P < 0.001$, **** means $P < 0.0001$ (n represent ears). (H) KI mice showed hind limb clasping at P270. (I) Representative images of hematein-eosin staining of sagittal brain sections. (J) The maximal treadmill stress test revealed that KI mice exhibited significantly reduced movement distances compared to WT mice at P270. **** means $P < 0.0001$(n = 5 mice/group). (K and L) Comparative analysis of the time spent (K) and speed (L) on uniformly accelerated rotating rods before falling for KI and WT mice at P270. * means $P < 0.05$, **** means $P < 0.0001$ (n = 5 mice/group). (M) Left panel: Representative images of Hematein-Eosin staining gastrocnemius muscle. Black arrows mean muscle atrophy. Right panel: Comparative analysis of the loss of muscle for KI and WT mice at P270 (n = 4 mice/group).
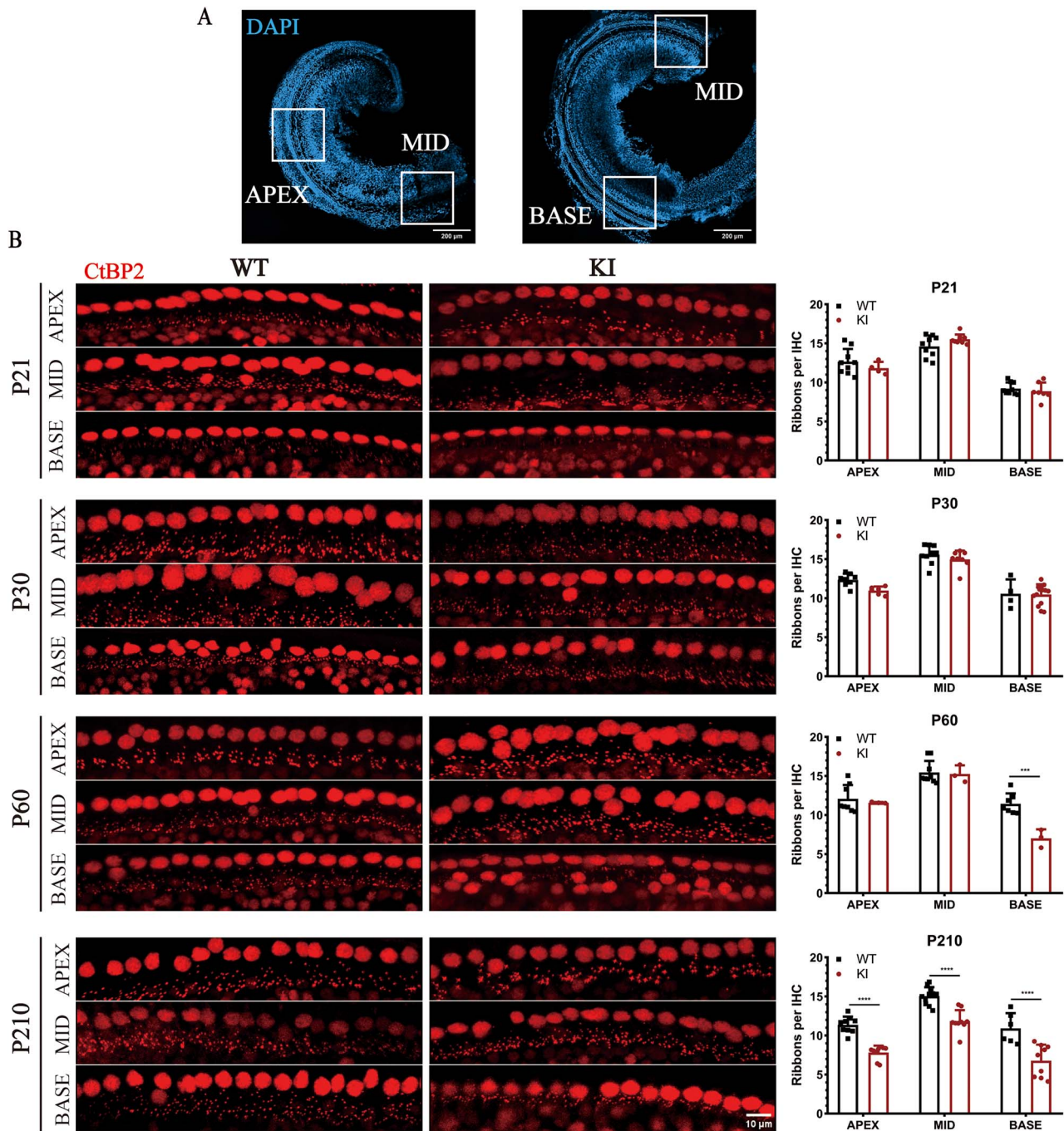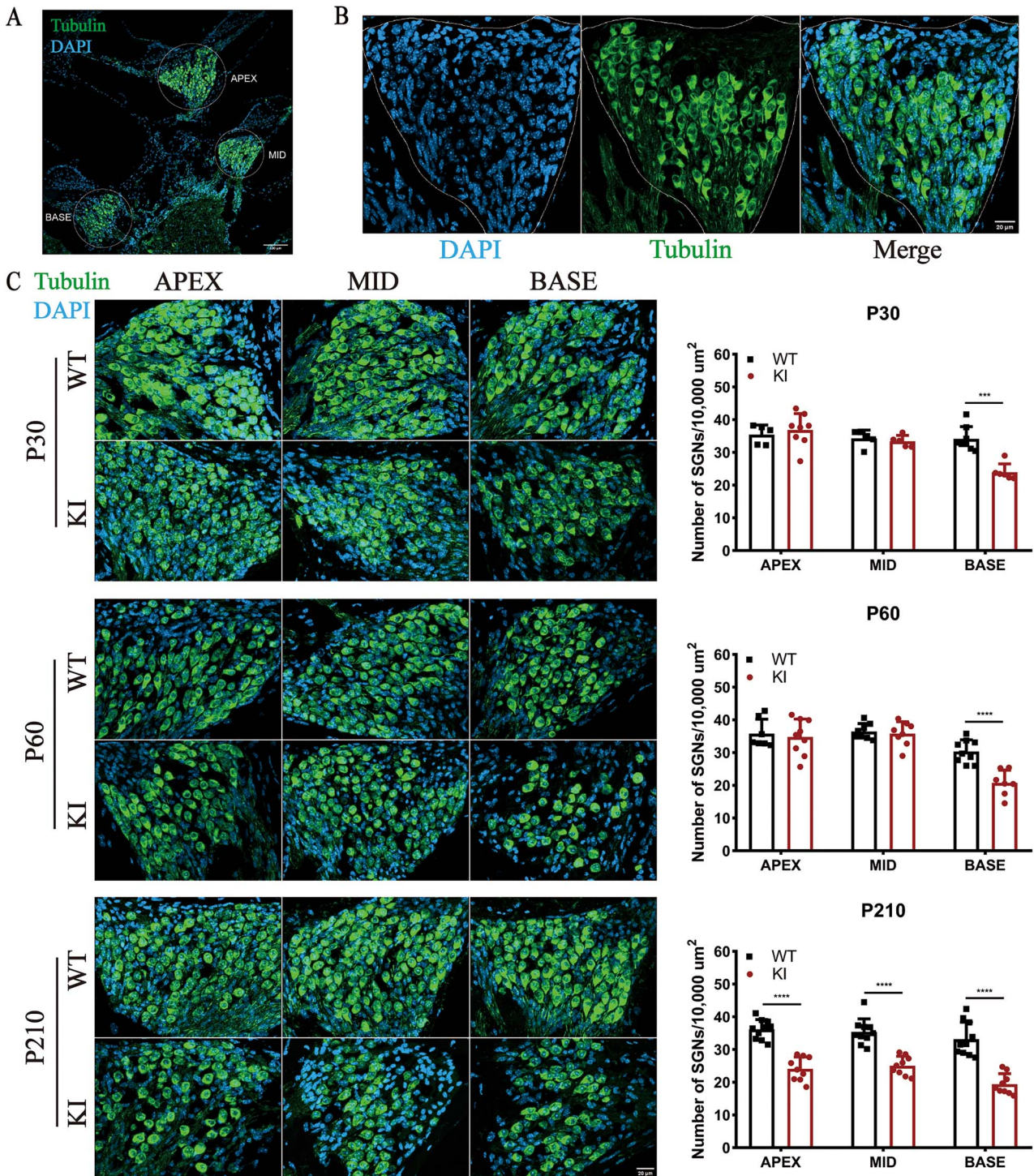
Figure 3. Pre-synaptic ribbons loss in the cochlea of *Aifm1* (p.R450Q) knock-in (KI) mice. (A) Schematic of the cochlear selected for ribbons counted. The number of ribbons was counted in apex, mid, and base. Scale bar = 200 μm. (B) There was no difference in ribbon counts between wild-type (WT) and KI mice at P21 and P30. It significantly decreased ribbons at the basal turn at P60. Further decreased at all turns at P210. Left panel: Immunofluorescence staining of ribbons (CtBP2) in all areas of the basilar membrane. Right panel: Quantification of the number of ribbons per inner hair cells (IHCs). Scale bar = 10 μm. *** means $P < 0.001$, **** means $P < 0.0001$. (n represents ears. P21 WT, n = 9; P21 KI, n = 4–9; P30 WT, n = 4–10; P30 KI, n = 6–14; P60 WT, n = 7–9; P60 KI, n = 3; P210 WT, n = 6–11; P210 KI, n = 9).

Aifm1 disrupts mitochondrial structure and causes demyelination of the auditory nerve

To investigate the effect of *Aifm1* variant on the mitochondrial and myelin status, we visualized the ultrastructural features of the auditory pathway under transmission electron microscopy (TEM) (Fig. 5A). The IHCs of the KI mice at P210 showed abnormal mitochondria lacking intact cristae (Fig. 5B), while the dendrites and axons of SGNs exhibited demyelination of auditory fibers with large vacuoles predominantly occupying the myelin sheath. Moreover, the mitochondria in the myelin sheath displayed abnormal morphology, including swelling and blurred cristae (Fig. 5C and D). These SGN abnormalities cause desynchronized firing of auditory nerves and AN. Additionally, SGNs of the KI mice at P210 showed loss of cytomembrane integrity and abnormal nuclear morphology, suggesting activation of cell death (Fig. 5E).

Figure 4. Spiral ganglion neuron cells (SGNs) loss in the cochlea of *Aifm1* (p.R450Q) knock-in (KI) mice. (A) Schematic of the cochlear selected for SGNs counted. The number of SGNs was counted in apex, mid, and base. Scale bar = 100 μm. (B) Schematic of the comparison area for the number of SGNs, with the area per unit area determined by the DAPI range. (C) Significantly decreased SGNs at the basal turn at P30 and decreased at P60. The number of SGNs decreased significantly at P210 in the whole turn. Left panel: Immunofluorescence staining of SGNs (tubulin) and DAPI in all cochlear parts. Scale bar = 20 μm. Right panel: Quantification of the numbers of SGNs. *** means $P < 0.001$, **** means $P < 0.0001$, (n represents ears. P30 WT, n = 5–8; P30 KI, n = 5–8; P60 WT, n = 7–9; P60 KI, n = 7–9; P210 WT, n = 10; P210 KI, n = 9).
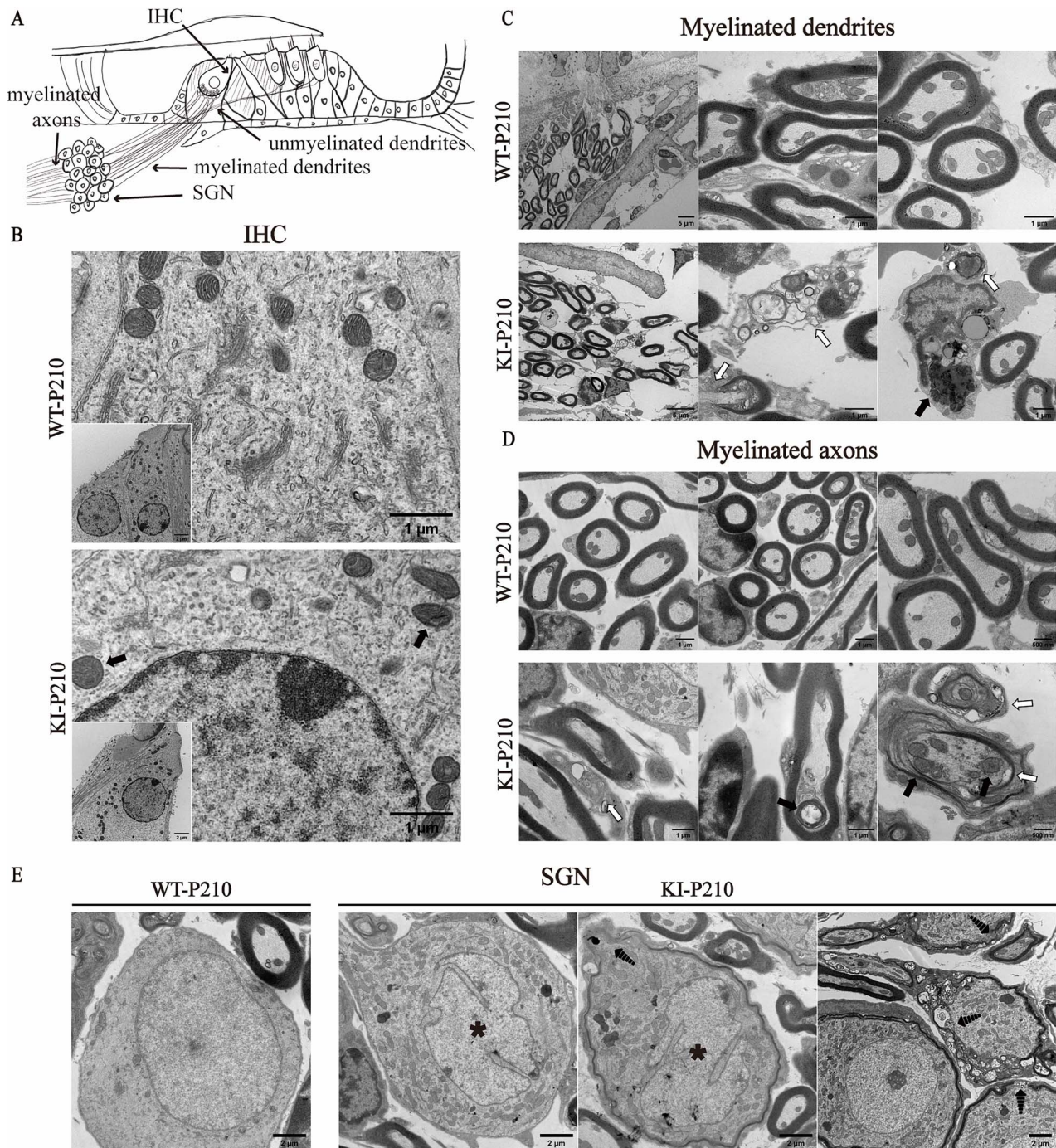
**Figure 5.** Auditory pathway transmission electron microscopy of *Aifm1* (p.R450Q) knock-in (KI) mice at P210. (A) Schematic representation of the auditory pathway. The inner hair cells (IHCs), myelinated dendrites, spiral ganglion cells (SGNs), and myelinated axons were from top to bottom. The diagram references Rance G and Starr A [2]. (B) Representative transmission electron micrographs (TEM) of IHC of WT and KI mice at P210 from four different mice. The IHCs of WT mice contained normal mitochondria with distinct cristae, while the mitochondria in KI mice were abnormal with fuzzy and unclear cristae. (C and D) Representative TEM images of myelinated dendrites and axons of WT and KI mice at P210 from three different mice. KI mice exhibited demyelination and completely degenerated, including intrinsic vacuole and myelin layers split and bulged (hollow arrows), and abnormal mitochondria, such as swollen and deformed (solid arrows) in the myelinated dendrites (C) and axons (D). (E) Representative TEM image of SGNs at P210 from four different mice of each group. KI mice exhibited abnormal morphology of nuclei of nerve cells (asterisk) and loss of cytomembrane integrity (dotted arrows).
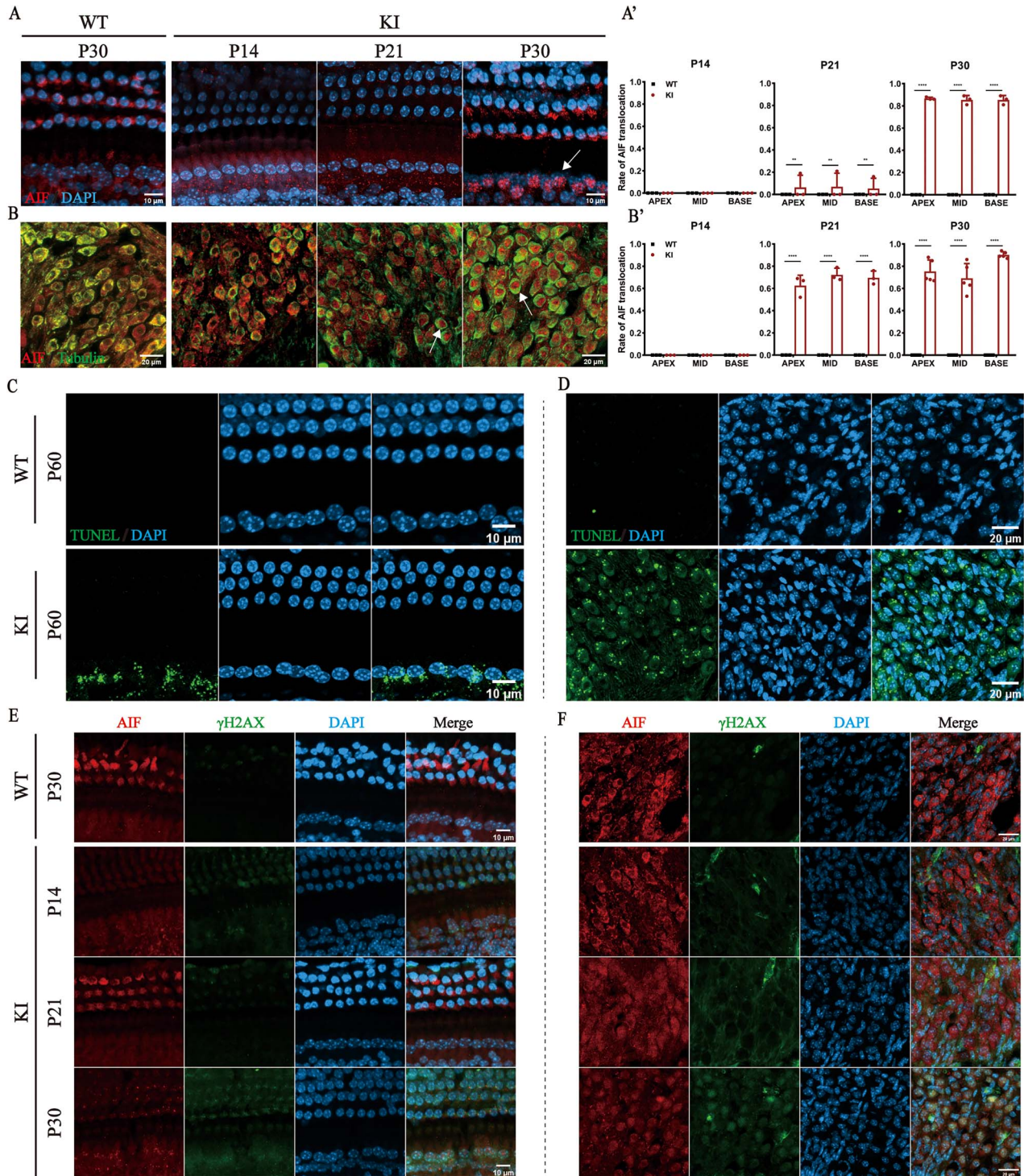
Figure 6. Dynamic translocation of AIF into the nucleus in the cochlea of *Aifm1* (p.R450Q) knock-in (KI) mice. (A) Representative of immunofluorescence staining images of AIF and DAPI in OHC of wild-type (WT) and KI mice. Nuclear translocation of AIF was predominantly observed at P30 in IHCs of KI mice, with no and little translocation at P14 and at P21, respectively. The white arrowhead is the nucleus of IHCs. Scale bars = 10 μm. ** means $P < 0.01$, **** means $P < 0.0001$. P14, P21, P30 WT and KI (n = 3 mice/group). (B) Representative of immunofluorescence staining images of AIF, tubulin, and DAPI in SGNs of WT and KI. AIF was predominantly translocated into the nucleus at P21 and P30, with no significant translocation observed at P14 in the SGN of KI mice. Scale bars = 20 μm. **** means $P < 0.0001$. P14, P21, WT and KI (n = 3 mice/group); P30 WT and KI (n = 5 mice/group). (C and D) Representative TUNEL staining of IHC, scale bars = 10 μm (C) and SGN, scale bars = 20 μm (D) in WT and KI mice at P60. (E) Representative immunofluorescence staining images of AIF, γH2AX, and DAPI in OHC of WT and KI, γH2AX was distributed around the nucleus but not inside it. In IHCs of KI, γH2AX translocated into the nucleus with AIF at P30. Scale bars = 10 μm. (F) Representative immunofluorescence staining images of AIF, γH2AX, and DAPI in SGNs of WT and KI mice, γH2AX translocated into the nucleus at P30 with AIF of KI mice. Scale bars = 20 μm.
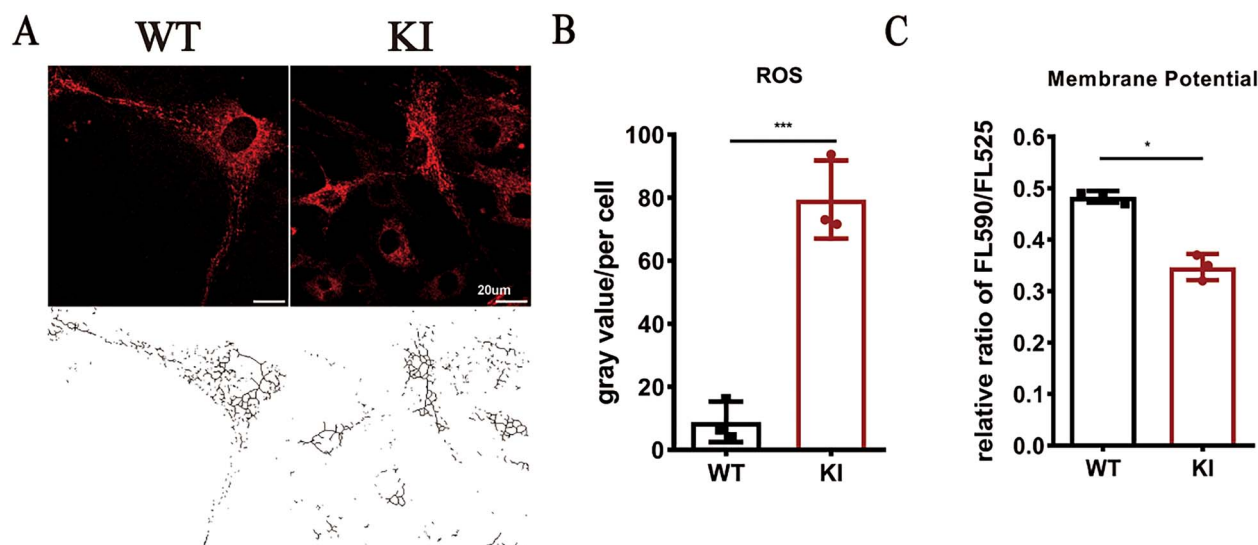
Figure 7. The mitochondrial function of the wild-type (WT) and *Aifm1* (p.R450Q) knock-in (KI) mice fibroblasts. (A) Mitotracker staining was used to examine the mitochondrial morphology of the live cells. Image J was used for network analysis to skeletonize the mitochondrial network. The images showed the fragmented mitochondrial network of the fibroblasts of KI mice. Scale bar = 20 μm. (B) MitoSOX staining (red) are shown. The fluorescence-related parameters remained consistent between WT and KI mice. *** means $P < 0.001$. (C) The mitochondrial membrane potential was analyzed using the JC-10 test system. *means $P < 0.05$.

Dynamic translocation of AIF into the nucleus in *Aifm1* (p.R450Q) knock-in mice

Nuclear translocation of AIF initially considered indispensable for caspase-independent apoptosis is an important marker. Therefore, using immunofluorescence analysis of whole-mounted cochlea, we observed a gradual translocation of AIF into the nucleus (Fig. 6A and B). AIF was distributed exclusively in the cytoplasm of OHCs, IHCs, and SGNs in WT mice at P30 (Fig. 1E and F). Whereas it was translocated into the nucleus of IHCs in KI mice a few at P21 and most at P30, but not at P14 (Fig. 6A). AIF translocation into the nucleus occurred earlier in SGNs than in the IHCs of KI mice from P21 onward (Fig. 6B). This phenomenon was not observed in the WT mice or OHCs of KI mice. Meanwhile, terminal deoxynucleotidyl transferase dUTP nick end labeling (TUNEL)-positive IHCs and SGNs were observed in P60 KI mice but not in the WT mice (Fig. 6C and D). Furthermore, γH2AX translocation into nucleus was detected specifically in SGNs and IHCs at P30 (Fig. 6E and F).

Aifm1 (p.R450Q) knock-in mice specific fibroblasts have mitochondrial dysfunction

AIF is responsible for maintaining OXPHOS and mitochondrial structure in healthy cells. Furthermore, mitochondrial dysfunction is the primary pathogenic mechanism underlying various neurodegenerative diseases. To assess mitochondrial function in vitro, we cultured KI mice-specific fibroblasts and examined their mitochondrial morphology. We observed that the KI fibroblasts had a fragmented mitochondrial network, while WT fibroblasts were filamentous (Fig. 7A). Subsequently, we examined the mitochondrial function in both KI and WT fibroblasts. The mitochondrial membrane potential of KI fibroblasts was 0.39 ± 0.06, and WT fibroblasts were 0.49 ± 0, $P = 0.0376$. The level of ROS production was calculated by measuring the gray value of each cell, KI fibroblasts was 79.39 ± 10.12, whereas for WT fibroblasts was 8.89 ± 5.26, $P = 0.0004$ (Fig. 7B and C).

Discussion

Here, we generated the first *Aifm1* KI mouse model of *AIFM1*-related AUNX1. We observed consistent phenotypes across individual mice carrying the disease-segregating *Aifm1* p.R450Q mutation. Our findings suggested that the KI mice exhibited late-onset hearing loss and muscle atrophy. Disruption of *Aifm1* led decreased cochlear expression of AIF. Pathologically, KI mice at P210 showed demyelination and abnormal cellular morphology of SGNs, and extensive loss of SGN and ribbons of IHC with AIF translocation into the nucleus.

Previously, we found that *AIFM1* (p.R451Q) as casual gene for AUNX1, which is mainly characterized by phenotypic features of AN. Hearing loss typically manifests in adolescence as the average onset age among affected individuals was 13 years [8, 9]. Here, the KI mice displayed late-onset hearing loss of all frequencies at P60, which marks the stage of sexual maturity for mice. This closely resembles the human hearing phenotype associated with *AIFM1* variations, as supported by clinical studies. There was no difference in the DPOAE performance between the KI and WT mice, indicating that OHC function remained unimpaired, thus satisfying the diagnostic criteria for AN. In addition to AN, AUNX1 might be associated with late-onset peripheral neuropathy [8, 9]. We observed that KI mice displayed muscle atrophy and motor function impairment, potentially resulting from peripheral neuropathy and innervation defects.

In both mice and humans, delayed hearing loss caused by *AIFM1* mutation warrants further investigation. The genes related to deafness are involved in the AN by influencing the morphology and development of the auditory pathway [2]. The subsequent loss of temporal accuracy or synchronization and erroneous neural representation of the auditory signal (induced by the loss of ribbons or SGNs) is the potential underlying mechanism of AN [5]. Our study found that *AIFM1* variations might contribute to the loss of ribbons loss and SGNs, and demyelination of SGNs in KI mice. The synapse comprises a pre-synaptic ribbon encircled by a halo of vesicles containing neurotransmitters within IHCs,

and a post-synaptic active zone on the cochlear nerve terminal equipped with glutamate receptors for the receiving the released neurotransmitters [32, 33]. Several animal studies confirmed that synapses are the most vulnerable components in both noise-exposed and age-related hearing loss [34, 35]. As AIF is the most vulnerable part of IHC, dysfunction leads to an extensive reduction in ribbons in KI mice at P210. Furthermore, after P45, the amplitude of ABR wave-I at 80 dB SPL in KI mice significantly declined at all frequencies (Supplementary Material 1, Fig. S2). As ABR wave-I is generated by the VIII nerve, which is near the cochlea [36], its suprathreshold amplitude can be a highly predictive indicator of synapse loss severity [5, 37]. The consistency between these two results indicates disruption of the synaptic ribbons and alterations in auditory function in KI mice, and all occurring late-onset.

Impairment of post-synaptic and auditory nerve fibers can occur at various locations along the auditory nerve [2]. The transmission of auditory information to the brain is compromised by impaired transmitter release from IHCs and synaptic dysfunction between SGNs and cochlear nucleus neurons. Knocking down AIF in SGNs caused impaired mitochondrial respiration and disrupted membrane potential, highlighting the crucial role of AIF in maintaining normal SGN function [38]. We found that the SGNs in KI mice reduced progressively, with an earlier onset compared to ribbon synapse loss (SGN loss initiated at P30 while ribbon synapse loss was not yet detected). Furthermore, demyelination and abnormal cellular morphology were evident in the myelinated SGNs of KI mice, indicating a fundamental pathological change of AN. In clinical studies, patients with these *AIFM1* variations showed lower apparent fiber density in the VIII nerve and degenerated auditory brainstem tracts compared to controls [39].

Several studies have demonstrated that cell death related to AIF majorly contributes to inner ear dysfunction [40, 41] and that nuclear translocation of AIF is an essential marker of cochlear cell death involving both SGNs and hair cells. Our findings indicate that after AIF was translocated into the IHCs and SGNs in KI mice, a few SGNs display a loss of cytomembrane integrity, as shown in the TEM images. This suggested that AIF-mediated cell death was activated, leading to a reduction in synapse and SGN numbers. This critical time point provides an important window for subsequent drug administration or related treatments. Meanwhile, γH2AX interacts specifically with AIF in the nucleus [19, 20], which is a sensitive marker of DNA double-strand breaks [42]. Genetic ablation of γH2AX conferred resistance to RCD [19]. We found that AIF and γH2AX were co-localized in the nuclei of IHCs and SGNs, suggesting that their interaction might play a role in KI mice. Furthermore, the TUNEL staining indicated that double strand breaks occur in both SGN and IHC of KI mice. Surprisingly, positive TUNEL staining was seen in the cytoplasm, possibly due to the occurrence of parthanatos, which causes loss of cytomembrane integrity, making positive staining leach out of the nucleus [21].

Mutations in genes related to mitochondria can alter antioxidant or mitochondrial functions, resulting in abnormal energy production, ROS production, or cell death [28]. Several neurodegenerative diseases have been associated with mitochondria dysfunction [43, 44], and the late onset of these diseases is aligned with the aging-related oxidative damage [28]. As *AIFM1* is related to mitochondrial function, fibroblasts derived from patients with *AIFM1* mutations showed reduced expression of complex subunits [11]. Mice with tissue-specific AIF deletions or a low AIF expression showed mitochondrial dysfunction. [24, 29, 45, 46]. We investigated the impact of *Aifm1* mutation on mitochondrial

function in vitro using skin fibroblasts from P0-P3 mice. Our findings indicated that *Aifm1* mutation causes mitochondrial dysfunctions, including reduced mitochondrial membrane potential and increased ROS production. Moreover, demyelination may be related to oxidative stress [47]. As myelin is composed of 80% lipids, it is highly susceptible to oxidative stress as lipids are prone to peroxidation in the presence of free radicals such as ROS [48, 49].

In summary, we generated an *Aifm1* KI mouse model with p.R450Q, which showed late-onset hearing loss and muscle atrophy, thus demonstrating the AUNX1 phenotype. Additionally, the *Aifm1* KI mouse model showed delayed loss of synaptic ribbons and SGNs and demyelination of auditory nerve fibers. AIF translocation into the cochlea and mitochondrial dysfunction is potentially the underlying pathogenic mechanism.

Materials and Methods
Animals
Briefly, the CRISPR/Cas9 system was used to generate the *Aifm1* (R450Q) KI mice based on the CBA/CaJ strain. Cas9 and guide mRNAs were co-injected into the zygotes and then injected into the uterus of pseudo-pregnant female mice (Supplementary Material 2). By crossing a founder mouse with WT CBA/CaJ mice, a colony with an *Aifm1* p.R450Q mutation was expanded. All experimental mice in this research were male. The mice were housed in groups of three to five per cage. They were allowed free access to food and water and maintained under standard conditions (room temperature: $22 \pm 2°C$; relative humidity: $55 \pm 10\%$) on a light: dark cycle of 12:12 h. All experiments were approved by the Committee of Laboratory Animals of Chinese People's Liberation Army General Hospital (approval No. 2022X18-26) on March 3, 2022, and were performed according to the National Institutes of Health guidelines.

Antibodies and reagents
The following antibodies were used: anti-AIF (ab32516, Abcam, USA; 1:300 for IF), anti-AIF (sc-13 116, Santa Cruz, USA; 1:1000 for WB), anti-CtBP2 (612044, BD, USA; 1:200 for IF), anti-γH2AX (JBW301, Merck, Germany; 1:300 for IF), anti-β3-Tubulin (MA1-118, Invitrogen, USA; 1:300 for IF), anti-β-actin (AF0003, Beyotime, China; 1:1000 for WB), Alexa Fluor 555-Phalloidin (A34055, Invitrogen; 1:1000 for IF), Alexa Fluor 488, 555, and 647 secondary antibodies (A-11008, A-11001, A-31572, A-31571, Invitrogen; 1:500 for IF), and anti-mouse horse radish peroxidase (HRP)-conjugated secondary antibodies (A0216, Beyotime; 1:5000 for WB). The reagents were: phosphate buffered saline (PBS) (P1010, Solarbio, China), 10% EDTA decalcifying solution (E1171, Solarbio), 4% paraformaldehyde (PFA) fixing solution (P0099, Beyotime), RIPA lysis buffer (P0013B, Beyotime), phenylmethanesulfonyl fluoride (PMSF) (36978, Thermo Fisher, USA), optimal cutting temperature compound (OCT) (4583, SAKURA, USA), Dulbecco's modified Eagle medium-high glucose (DMEM-HG) (11965092, Gibco, USA), fetal bovine serum (FBS) (10099141C, Gibco), penicillin-streptomycin (15140122, Gibco), and DAPI (ZLI-9557, ZSGB-BIO, China).

Functional hearing assessments
All the assessments were performed under anesthesia using intraperitoneal injection of 1% pentobarbital sodium (0.1 ml/10 g). ABR was measured at P21, P30, P45, P60 and P210. DPOAE was recorded at P30, P45, P60, and P270. ABR and DPOAE were performed using the RZ6 Acoustic System (Tucker-Davis Technologies, Alachua, FL, USA).

ABR. Ground, reference, and recording electrodes were inserted subcutaneously at the inferior posterior margin of the contralateral ear, the inferior posterior margin of the giving ear, and at the midpoint of the line connecting the two ears of mice, respectively. ABR tests were performed using Click and tone bursts (8, 16, 24, and 32 kHz). The lowest stimulus level at which a repeatable morphology could be recognized in the response waveform was used to determine the threshold.

DPOAE. Two primary tones of frequency f1 and f2 with a constant frequency ratio f2/f1 = 1.2 were generated. The distortion product at 2f1-f2 was measured for each tested frequency.

Behavioral assessments
Rotarod

Using a mouse rotary rod fatigue apparatus (ZH-600B, Zhongshi, China, the mice were trained for 1, 2, and 3 min with speeds of 4, 10, and 30 rpm. During the test, the mice were placed on a rotating rod with an initial speed of 4 rpm and an acceleration of 20 rpm/min^2 until a maximum speed of 40 rpm was reached. The speed and time of the rotating rod were recorded when the mice fell.

Treadmill assessment

After three-day training, a formal test was conducted using an animal treadmill (ZH-PT/5S, Huazheng, China) at a consistent speed of 15 m/min and with a treadmill tilt angle of 0°. The movement distance of the mice from the beginning of exercise to fatigue was recorded. The fatigue standard was that the mice were always in the back 1/3 of the runway.

Morphological assessments
Basilar membrane

After euthanizing the mice, their cochlea was removed and fixed in 4% PFA overnight at 4°C. Then, they were placed in 10% EDTA for 2.5 h at room temperature to remove the basilar membrane. The basilar membrane was incubated in a blocking buffer containing 10% goat serum and PBS containing 0.66% Triton X-100 for 2 h at room temperature, followed by overnight immunostaining at 4°C with primary antibodies. Then, the secondary antibodies were incubated for 2 h at room temperature. Finally, the cells were incubated with DAPI. Fluorescent images were observed on a Zeiss LSM980 laser confocal microscope.

SGNs

The cochlea was fixed in 4% PFA overnight at 4°C,transferred to 10% EDTA for 24 h at room temperature, soaked in 15% and 30% sucrose solutions for 2 h, and finally soaked in OCT. for 2 h, and sectioned at a thickness of 10 μm (CM1860, Leica, Germany). The preparatory steps for immunofluorescence were the same as that for the basilar membrane.

Cerebellum and gastrocnemius

After the specimens were quickly fixed, the cerebellum and gastrocnemius muscle were paraffin sectioned. The nucleus and cytoplasm were stained with hematoxylin and eosin, respectively. After dehydration and sealing, the images were obtained using a microscope (DM3000, Leica).

TEM

Cochleae were quickly immersed and dissected in PBS containing 2.5% glutaraldehyde. The cochlea was fixed for 2 h in a preparation containing 2.5% glutaraldehyde and phosphate buffer. After rinsing with 0.1 M phosphate, they were fixed in 1% osmium fixative, and rinsed again. Gradient dehydration was performed using ethanol and propanol. Embedding was done in stages using pure acetone and various embedding solution ratios. Then, the samples were fixed successively at 37°C, 45°C, and 60°C ovens before being sliced into 70 nm-thick ultra-thin sections and then examined with a JEOL JEM-1230 transmission electron microscope (80 KV).

TUNEL staining

TUNEL assay was performed using an in situ cell death detection kit (11684795910, Merck). Specimens were fixed in 4% PFA for 20 min. Then, the TUNEL reaction mixture was added and incubated in the dark for 2 h at 37°C. After washing with PBS, the slides were sealed with DAPI.

Western blot

The cochlear tissues were lysed with RIPA lysis buffer containing protease, phosphatase inhibitors, and PMSF, on ice. The sample protein concentration was measured using the BCA Protein Concentration Assay Kit (A53225, Thermo Fisher). The protein lysates were separated by SDS-PAGE, transferred to the PVDF membranes (Millipore, Massachusetts, USA), and blocked with 8% milk for 1 h. The membranes were incubated overnight at 4°C with primary antibodies and then for 2 h at room temperature with a secondary antibody. After pressing the membranes with an X-ray in the dark to obtain the target protein bands were obtained.

Determination of mitochondrial function
Mouse fibroblast primary culture

The skin of mice in P1-3 was cut with sterile scissors and placed in a medium composed of DMEM, FBS, and penicillin-streptomycin. After removing the excess tissue, the fibroblasts were cultured in the medium. Two strains of WT and KI cells were kept at 37°C in a 5% CO_2 incubator.

Mitochondrial function assessments

Mitochondrial function was assessed using ROS (M36008, Invitrogen) and mitochondrial membrane potential (ab112134, Abcam) assays, according to the manufacturer's instructions and the reported guidelines [50]. Cells were stained with 100 nM of Mito-Tracker (M22425, Invitrogen) and live cells were imaged using an LSM980 laser scanning confocal microscope.

Data processing and statistical analysis

The data was presented as mean ± SD. Using GraphPad Prism 8 software, the data was statistically analyzed using the Two-way ANOVA or T-test. Significant *P* values were indicated: * means $P < 0.05$, ** means $P < 0.01$, *** means $P < 0.001$, and**** means $P < 0.0001$. All experiments were independently repeated at least thrice.

Supplementary data

Supplementary data is available at *HMG Journal* online.

Funding

References

1. Sininger YS. Identification of auditory neuropathy in infants and children. *Semin Hear* 2002;**23**:193–200.

2. Rance G, Starr A. Pathophysiological mechanisms and functional hearing consequences of auditory neuropathy. *Brain J Neurol* 2015;**138**:3141–58.

3. Starr A, Picton TW, Sininger Y. *et al.* Auditory neuropathy. *Brain J Neurol* 1996;**119**:741–53.

4. Rance G. Auditory neuropathy/dys-synchrony and its perceptual consequences. *Trends Amplif* 2005;**9**:1–43.

5. Moser T, Starr A. Auditory neuropathy—neural and synaptic mechanisms. *Nat Rev Neurol* 2016;**12**:135–49.

6. Huang Y, Yang J, Duan M. Auditory neuropathy: from etiology to management. *Curr Opin Otolaryngol Head Neck Surg* 2022;**30**:332–8.

7. Manchaiah VK, Zhao F, Danesh AA. *et al.* The genetic basis of auditory neuropathy spectrum disorder (ANSD). *Int J Pediatr Otorhinolaryngol* 2011;**75**:151–8.

8. Wang QJ, Li QZ, Rao SQ. *et al.* AUNX1, a novel locus responsible for X linked recessive auditory and peripheral neuropathy, maps to Xq23-27.3. *J Med Genet* 2006;**43**:e33.

9. Zong L, Guan J, Ealy M. *et al.* Mutations in apoptosis-inducing factor cause X-linked recessive auditory neuropathy spectrum disorder. *J Med Genet* 2015;**52**:523–31.

10. Wang H, Bing D, Li J. *et al.* High frequency of *AIFM1* variants and phenotype progression of auditory neuropathy in a Chinese population. *Neural Plast* 2020;**2020**:5625768.

11. Ghezzi D, Sevrioukova I, Invernizzi F. *et al.* Severe X-linked mitochondrial encephalomyopathy associated with a mutation in apoptosis-inducing factor. *Am J Hum Genet* 2010;**86**:639–49.

12. Ardissone A, Piscosquito G, Legati A. *et al.* A slowly progressive mitochondrial encephalomyopathy widens the spectrum of *AIFM1* disorders. *Neurology* 2015;**84**:2193–5.

13. Bogdanova-Mihaylova P, Alexander MD, Murphy RP. *et al.* Clinical spectrum of *AIFM1*-associated disease in an Irish family, from mild neuropathy to severe cerebellar ataxia with colour blindness. *J Peripher Nerv Syst* 2019;**24**:348–53.

14. Bano D, Prehn JHM. Apoptosis-inducing factor (AIF) in physiology and disease: the tale of a repented natural born killer. *EBioMedicine* 2018;**30**:29–37.

15. Susin SA, Lorenzo HK, Zamzami N. *et al.* Molecular characterization of mitochondrial apoptosis-inducing factor. *Nature* 1999;**397**:441–6.

16. Andrabi SA, Dawson TM, Dawson VL. Mitochondrial and nuclear cross talk in cell death: parthanatos. *Ann N Y Acad Sci* 2008;**1147**:233–41.

17. Galluzzi L, Vitale I, Aaronson SA. *et al.* Molecular mechanisms of cell death: recommendations of the nomenclature committee on cell death 2018. *Cell Death Differ* 2018;**25**:486–541.

18. Wang Y, An R, Umanah GK. *et al.* A nuclease that mediates cell death induced by DNA damage and poly(ADP-ribose) polymerase-1. *Science (New York, NY)* 2016;**354**:82.

19. Artus C, Boujrad H, Bouharrour A. *et al.* AIF promotes chromatinolysis and caspase-independent programmed necrosis by interacting with histone H2AX. *EMBO J* 2010;**29**:1585–99.

20. Baritaud M, Boujrad H, Lorenzo HK. *et al.* Histone H2AX: the missing link in AIF-mediated caspase-independent programmed necrosis. *Cell Cycle* 2010;**9**:3166–73.

21. Park H, Kam TI, Dawson TM. *et al.* Poly (ADP-ribose) (PAR)-dependent cell death in neurodegenerative diseases. *Int Rev Cell Mol Biol* 2020;**353**:1–29.

22. Joza N, Pospisilik JA, Hangen E. *et al.* AIF: not just an apoptosis-inducing factor. *Ann N Y Acad Sci* 2009;**1171**:2–11.

23. Meyer K, Buettner S, Ghezzi D. *et al.* Loss of apoptosis-inducing factor critically affects MIA40 function. *Cell Death Dis* 2015;**6**:e1814.

24. Hangen E, Féraud O, Lachkar S. *et al.* Interaction between AIF and CHCHD4 regulates respiratory chain biogenesis. *Mol Cell* 2015;**58**:1001–14.

25. Cheung EC, Joza N, Steenaart NA. *et al.* Dissociating the dual roles of apoptosis-inducing factor in maintaining mitochondrial structure and apoptosis. *EMBO J* 2006;**25**:4061–73.

26. Joza N, Susin SA, Daugas E. *et al.* Essential role of the mitochondrial apoptosis-inducing factor in programmed cell death. *Nature* 2001;**410**:549–54.

27. Brown D, Yu BD, Joza N. *et al.* Loss of Aif function causes cell death in the mouse embryo, but the temporal progression of patterning is normal. *PNAS* 2006;**103**:9918–23.

28. Klein JA, Longo-Guess CM, Rossmann MP. *et al.* The harlequin mouse mutation downregulates apoptosis-inducing factor. *Nature* 2002;**419**:367–74.

29. Vahsen N, Candé C, Brière JJ. *et al.* AIF deficiency compromises oxidative phosphorylation. *EMBO J* 2004;**23**:4679–89.

30. Bénit P, Goncalves S, Dassa EP. *et al.* The variability of the harlequin mouse phenotype resembles that of human mitochondrial-complex I-deficiency syndromes. *PLoS One* 2008;**3**:e3208.

31. Wischhof L, Gioran A, Sonntag-Bensch D. *et al.* A disease-associated *Aifm1* variant induces severe myopathy in knockin mice. *Mol Metab* 2018;**13**:10–23.

32. Wichmann C, Moser T. Relating structure and function of inner hair cell ribbon synapses. *Cell Tissue Res* 2015;**361**:95–114.

33. Glowatzki E, Fuchs PA. Transmitter release at the hair cell ribbon synapse. *Nat Neurosci* 2002;**5**:147–54.

34. Kujawa SG, Liberman MC. Adding insult to injury: cochlear nerve degeneration after "temporary" noise-induced hearing loss. *J Neurosci* 2009;**29**:14077–85.

35. Kujawa SG, Liberman MC. Synaptopathy in the noise-exposed and aging cochlea: primary neural degeneration in acquired sensorineural hearing loss. *Hear Res* 2015;**330**:191–9.

36. Starr A, Hamilton AE. Correlation between confirmed sites of neurological lesions and abnormalities of far-field auditory brainstem responses. *Electroencephalogr Clin Neurophysiol* 1976;**41**:595–608.

37. Liberman MC, Kujawa SG. Cochlear synaptopathy in acquired sensorineural hearing loss: manifestations and mechanisms. *Hear Res* 2017;**349**:138–47.

38. Zong L, Zhao J, Wu W. *et al.* AIF knockdown induce apoptosis and mitochondrial dysfunction in cochlear spiral ganglion neurons in vitro. *Mol Med Rep* 2020;**21**:1910–20.

39. Zanin J, Dhollander T, Rance G. *et al.* Fiber-specific changes in white matter microstructure in individuals with X-linked auditory neuropathy. *Ear Hear* 2020;**41**:1703–14.

40. Shen H, Liu W, Geng Q. *et al.* Age-dependent up-regulation of HCN channels in spiral ganglion neurons coincide with hearing loss in mice. *Front Aging Neurosci* 2018;**10**:353.

41. Han W, Shi X, Nuttall AL. AIF and endoG translocation in noise exposure induced hair cell death. *Hear Res* 2006;**211**:85–95.

42. Kinner A, Wu W, Staudt C. *et al.* Gamma-H2AX in recognition and signaling of DNA double-strand breaks in the context of chromatin. *Nucleic Acids Res* 2008;**36**:5678–94.

43. Beal MF. Mitochondria take center stage in aging and neurodegeneration. *Ann Neurol* 2005;**58**:495–505.

44. Cassarino DS, Bennett JP Jr. An evaluation of the role of mitochondria in neurodegenerative diseases: mitochondrial mutations and oxidative pathology, protective nuclear responses, and cell death in neurodegeneration. *Brain Res* 1999;**29**: 1–25.

45. Joza N, Oudit GY, Brown D. *et al.* Muscle-specific loss of apoptosis-inducing factor leads to mitochondrial dysfunction, skeletal muscle atrophy, and dilated cardiomyopathy. *Mol Cell Biol* 2005;**25**:10261–72.

46. Pospisilik JA, Knauf C, Joza N. *et al.* Targeted deletion of AIF decreases mitochondrial oxidative phosphorylation and protects from obesity and diabetes. *Cell* 2007;**131**:476–91.

47. Ravera S, Bartolucci M, Cuccarolo P. *et al.* Oxidative stress in myelin sheath: the other face of the extramitochondrial oxidative phosphorylation ability. *Free Radic Res* 2015;**49**:1156–64.

48. Bongarzone ER, Pasquini JM, Soto EF. Oxidative damage to proteins and lipids of CNS myelin produced by in vitro generated reactive oxygen species. *J Neurosci Res* 1995;**41**:213–21.

49. van Hameren G, Campbell G, Deck M. *et al.* In vivo real-time dynamics of ATP and ROS production in axonal mitochondria show decoupling in mouse models of peripheral neuropathies. *Acta Neuropathol* 2019;**7**:86.

50. Qiu Y, Wang H, Fan M. *et al.* Impaired AIF-CHCHD4 interaction and mitochondrial calcium overload contribute to auditory neuropathy spectrum disorder in patient-iPSC-derived neurons with *AIFM1* variant. *Cell Death Dis* 2023;**14**:375.